Author(s): Lehikoinen, Antti & Ikaheimo, Jouni & Arkkio, Antero & Belahcen, Anouar

Title: Domain Decomposition Approach for Efficient Time-Domain Finite-Element Computation of Winding Losses in Electrical Machines

Year: 2017

Version: Post print

Please cite the original version:

Lehikoinen, Antti & Ikaheimo, Jouni & Arkkio, Antero & Belahcen, Anouar. 2017. Domain Decomposition Approach for Efficient Time-Domain Finite-Element Computation of Winding Losses in Electrical Machines. IEEE Transactions on Magnetics. Volume 53, Issue 5. 1-9. ISSN 0018-9464 (printed). DOI: 10.1109/tmag.2017.2681045.

Domain Decomposition Approach for Efficient Time-Domain Finite Element Computation of Winding Losses in Electrical Machines

Antti Lehikoinen[1], Jouni Ikäheimo[2], Antero Arkkio[1], and Anouar Belahcen[1]
[1]Aalto University, Dept. of Electrical Engineering and Automation, P.O. Box 13000, FI-00076 Espoo, Finland
[2]ABB Oy, Vaasa 65101, Finland

Finite element analysis of winding losses in electrical machines can be computationally uneconomical. Computationally lighter methods often place restrictions on the winding configuration or have been used for time-harmonic problems only. This paper proposes a domain decomposition type approach for solving this problem. The slots of the machine are modelled by their impulse response functions and coupled together with the rest of the problem. The method places no restrictions on the winding and naturally includes all resistive AC loss components. The method is then evaluated on a 500 kW induction motor. According to the simulations, the method yields precise results 70–100 faster compared to the established finite element approach.

Index Terms—**Finite element analysis, eddy currents, proximity effects, reduced order systems.**

I. Introduction

Accurate prediction of resistive winding losses can be crucial for the design and optimization of both high-efficiency and high-performance electrical machines. Due to complex geometries, numerical finite element analysis is usually required for this purpose. However, a dense mesh is typically imperative for sufficient accuracy, resulting in long computation times. This problem is further compounded by the widespread use of frequency converter supply, the analysis of which requires a short time-step length to accurately model the effects of supply harmonics.

Winding losses can be divided into two components: skin- and proximity effects, and circulating currents. The former two refer to an uneven current distribution *inside* a particular conductor, due to the time-varying field generated by either the same conductor or nearby ones. Typically, the proximity effects dominate. By contrast, circulating currents refer to an uneven distribution of *total current* between parallel conductors.

Several approaches have been proposed for the analysis of proximity effect, most based on homogenization of the winding [1]–[8]. However, practically all research has focused on series-connected coils, or otherwise ignored the circulating current effects altogether. Their inclusion would require some further study. Furthermore, homogenization approaches are normally based on a minimal symmetric region, so a regular packing of conductors is required. Finally, their accuracy can suffer near the borders of the homogenized region, although it can be improved by subproblem modelling [9]. By contrast, research on circulating currents has mostly utilized brute-force analysis on problems with relatively few conductors or ignored the proximity effects altogether [10]–[19]. Some analytical methods have also been studied, along with brute-force approaches [20]–[23].

This paper proposes a domain decomposition type approach for computationally efficient winding loss analysis in time-domain. The slots are modelled by their pre-computed impulse response functions, and coupled together with the rest of the problem domain on the boundary. All three loss components are naturally taken into account, and the method can be applied to linear and nonlinear problems both. Furthermore, there are no restrictions on the winding configuration or geometry. The proposed method has been inspired by [24], but addresses many of its limitations related to analysing electrical machines. For instance, the method can be used with arbitrary conductor packings and slot shapes, and has been extended to time-domain.

The performance of the proposed method is evaluated on a 500 kW induction motor with a stranded stator winding. A 100-fold speed-up is observed in time-harmonic analysis, compared to a reference solution. In time-stepping, the factor is 70. In both cases, the method yields very accurate results.

According to the simulations, the analyzed motor can exhibit significant circulating current losses, especially when supplied with a pulse-width modulated voltage source. These losses appear to be highly sensitive to the exact winding configuration, i.e. whether or not the parallel strands are transposed from slot to slot.

II. Basic Theory

This section briefly presents some basic finite element (FE) theory, necessary for understanding the method proposed in the next section. The well-known two-dimensional A-V formulation will be used [25]. After discretization, the problem consists of the nodal vector potentials $\mathbf{a}$, the voltages $\mathbf{u}$ over the conductors, plus a set of linearly independent currents (typically loop currents) $\mathbf{i}$. In time-domain, the problem can

Manuscript received December 9, 2016; revised February 11, 2017; accepted March 7, 2017. Corresponding author: A. Lehikoinen (email: antti.lehikoinen@aalto.fi).
Color versions of one or more of the figures in this paper are available online at http://ieeexplore.ieee.org.
DOI: 10.1109/TMAG.2017.2681045

be expressed as

$$\begin{bmatrix} \mathbf{S}+\mathbf{M}\frac{\mathrm{d}}{\mathrm{d}t} & \mathbf{C}_\mathrm{J} & \mathbf{0} \\ \mathbf{C}_\mathrm{E}\frac{\mathrm{d}}{\mathrm{d}t} & -\mathbf{I} & \mathbf{RL} \\ \mathbf{0} & \mathbf{L}^\mathrm{T} & \mathbf{Z} \end{bmatrix} \begin{bmatrix} \mathbf{a} \\ \mathbf{u} \\ \mathbf{i} \end{bmatrix} = \begin{bmatrix} \mathbf{0} \\ \mathbf{0} \\ \mathbf{u}_\mathrm{s} \end{bmatrix}. \tag{1}$$

$\mathbf{S}$ and $\mathbf{M}$ are the well-known stiffness and mass matrices and $\mathbf{u}_\mathrm{s}$ is the sum of supply voltages for each current loop. Furthermore, the matrices $\mathbf{C}_\mathrm{J}$ and $\mathbf{C}_\mathrm{E}$

$$[\mathbf{C}_\mathrm{J}]_{ij} = \frac{-\sigma}{l_\mathrm{e}} \int\limits_{\Omega_j^\mathrm{c}} \varphi_i \mathrm{d}S \tag{2}$$

$$[\mathbf{C}_\mathrm{E}]_{ij} = R_i \int\limits_{\Omega_i^\mathrm{c}} \varphi_j \mathrm{d}S \tag{3}$$

are used to consider the current density and average back-emf in the conductors, with their cross-sectional domains denoted by Ω_i^c. The effective length and conductivity are denoted by l_e and σ, whereas the shape function associated with the node i is φ_i. The diagonal matrix $\mathbf{R}$ contains the DC-resistances R_i of each conductor i, and the end-winding impedances are collected in the matrix $\mathbf{Z}$. Finally, the loop matrix $\mathbf{L}$ describes the winding topology, with the entries

$$[\mathbf{L}]_{ij} = \begin{cases} 1 & \text{current } j \text{ flows through conductor } i \text{ forwards} \\ -1 & \text{current } j \text{ flows through conductor } i \text{ backwards} \\ 0 & \text{otherwise.} \end{cases} \tag{4}$$

III. Proposed Decomposition Approach

This section describes the proposed domain decomposition approach. An electrical machine with a stranded stator winding is used as an example application in this paper, although the method could easily be applied for modeling other types of windings as well. The method is based on the elimination of the dense slot mesh from the problem, yielding a significant reduction in the number of unknowns. Several details are discussed in their respective subsections, such as different initial conditions and loss computation. A brief comparison to existing work is also presented.

For the remainder of this paper, the following terminology is adopted. The slots shall be referred to as *slave domain*, whereas the rest of the machine will be called *main domain*. The terms slave problem and main problem will be used correspondingly. Finally, the term *reference* shall be used to refer to the established FE approach without any dimensionality reduction techniques utilized.

A single slot segment of an electrical machine is used as an example, illustrated in Fig. 1. This domain is easily divided into the main and slave domains, with the boundary highlighted in blue. The winding inside the slot is stranded, with the conductors illustrated with the red circles. This requires a very dense mesh, increasing the computational cost. By contrast, the main domain could be easily modelled with a much coarser mesh shown in Fig. 1. This fact can be exploited by means of a decomposition approach shown next.

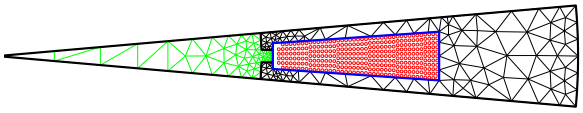

Fig. 1. Example segment.

A. Method Description

Next, the basic principle of the proposed approach is presented. Both the main and slave domains of the example problem are meshed independently. The main domain is governed by simply

$$\mathbf{Sa} = \mathbf{f}, \tag{5}$$

whereas the equations for the slave domain are are

$$\tilde{\mathbf{M}}\frac{\mathrm{d}}{\mathrm{d}t}\tilde{\mathbf{a}} + \tilde{\mathbf{S}}\tilde{\mathbf{a}} + \tilde{\mathbf{C}}_\mathrm{J}\tilde{\mathbf{u}} = \mathbf{0} \tag{6}$$

$$\tilde{\mathbf{C}}_\mathrm{E}\frac{\mathrm{d}}{\mathrm{d}t}\tilde{\mathbf{a}} - \tilde{\mathbf{u}} + \mathbf{RL}\tilde{\mathbf{i}} = \mathbf{0} \tag{7}$$

$$\mathbf{L}^\mathrm{T}\tilde{\mathbf{u}} + \mathbf{Z}\tilde{\mathbf{i}} = \mathbf{u}_\mathrm{s}. \tag{8}$$

The quantities associated with the slot domain are identified with the tilde notation $\tilde{\mathbf{a}}$, whereas un-tilded ones refer to the main domain. Zero initial conditions at $t = 0$ are assumed for now. The length of $\mathbf{a}$ and $\tilde{\mathbf{a}}$ are N_m and N_s, respectively, with $N_\mathrm{m} << N_\mathrm{s}$. The numbers of voltages and currents are N_u and N_i.

In addition to (5)–(8), the continuity between $\tilde{\mathbf{a}}$ and $\mathbf{a}$ on the main-slave boundary has to be enforced. For that purpose, let us denote the discrete potentials of the main mesh nodes that are located on the boundary by $\partial\mathbf{a}$, of length n_mb. Likewise, the n_sb boundary nodes of the slave mesh are denoted by $\partial\tilde{\mathbf{a}}$.

Then, the continuity requirement between the slot and main domains for the discrete problem can be expressed as

$$\mathbf{P}_\mathrm{ms}\partial\mathbf{a} - \partial\tilde{\mathbf{a}} = \mathbf{0}. \tag{9}$$

The $n_\mathrm{sb} \times n_\mathrm{mb}$ matrix $\mathbf{P}_\mathrm{ms}$ can be formed by e.g. the mortar method, or by following the authors' polynomial interpolation approach in [26]. Both methods have been observed to yield good results [27], [28], but a thorough comparison is beyond the scope of this paper. Like was done in [29], let us also define the selection matrices $\mathbf{B}$ and $\tilde{\mathbf{B}}$ (of size $n_\mathrm{mb} \times N_\mathrm{m}$ and $n_\mathrm{sb} \times N_\mathrm{s}$) for extracting the boundary nodes

$$\partial\mathbf{a} = \mathbf{Ba} \tag{10}$$

$$\partial\tilde{\mathbf{a}} = \tilde{\mathbf{B}}\tilde{\mathbf{a}}. \tag{11}$$

In other words, $[\mathbf{B}]_{ij} = 1$ if node j of the main mesh is also the i^th entry in $\partial\mathbf{a}$, and zero otherwise.

As is well known, the continuity (9) can be enforced with Lagrange multipliers $\mathbf{h}$. The $n_\mathrm{sb} \times 1$ vector $\mathbf{h}$ can be understood as the discrete equivalent of the normal derivative of the vector potential on the boundary, i.e. the tangential component of the

magnetic field strength (e.g. [30]–[32]). Eqs. (5)–(8) and (9) are combined into the augmented system

$$\begin{bmatrix} \mathbf{S} & 0 & 0 & 0 & (\mathbf{P}_{\mathrm{ms}}\mathbf{B})^{\mathrm{T}} \\ 0 & \tilde{\mathbf{S}} + \tilde{\mathbf{M}}\frac{\mathrm{d}}{\mathrm{d}t} & \tilde{\mathbf{C}}_{\mathrm{J}} & 0 & -\tilde{\mathbf{B}}^{\mathrm{T}} \\ 0 & \tilde{\mathbf{C}}_{\mathrm{E}}\frac{\mathrm{d}}{\mathrm{d}t} & -\mathbf{I} & \mathbf{R}\mathbf{L}\tilde{\mathbf{i}} & 0 \\ 0 & 0 & \mathbf{L}^{\mathrm{T}} & \mathbf{Z} & 0 \\ \mathbf{P}_{\mathrm{ms}}\mathbf{B} & -\tilde{\mathbf{B}}^{\mathrm{T}} & 0 & 0 & 0 \end{bmatrix} \begin{bmatrix} \mathbf{a} \\ \tilde{\mathbf{a}} \\ \tilde{\mathbf{u}} \\ \tilde{\mathbf{i}} \\ \mathbf{h} \end{bmatrix} = \begin{bmatrix} \mathbf{f} \\ \mathbf{0} \\ \mathbf{0} \\ \mathbf{u}_{\mathrm{s}} \\ \mathbf{0} \end{bmatrix}. \tag{12}$$

The entire system is time-dependent, including the multipliers $\mathbf{h}$.

Now, as will be shown in Section III-B, $\mathbf{h}$ and $\tilde{\mathbf{u}}$ can be written as

$$\mathbf{h} = \mathbf{C}_{\mathrm{ha}}\partial\mathbf{a} + \mathbf{C}_{\mathrm{hi}}\tilde{\mathbf{i}} + \mathbf{c}_{\mathrm{h}} \tag{13}$$

$$\tilde{\mathbf{u}} = \mathbf{C}_{\mathrm{ua}}\partial\mathbf{a} + \mathbf{C}_{\mathrm{ui}}\tilde{\mathbf{i}} + \mathbf{c}_{\mathrm{u}}, \tag{14}$$

with some known matrices $\mathbf{C}_{\mathrm{ha}}, \mathbf{C}_{\mathrm{hi}}, \mathbf{C}_{\mathrm{ua}}, \mathbf{C}_{\mathrm{ui}}$ and vectors $\mathbf{c}_{\mathrm{h}}$, $\mathbf{c}_{\mathrm{u}}$. Eq. (13) can be understood as a discrete Dirichlet-to-Neumann map, i.e. a mapping from the boundary potentials and currents to the discrete fluxes $\mathbf{h}$.

With (13), we see that block-rows 1 and 4 in (12) can be fully decoupled from the rest of the problem, resulting in the smaller system

$$\begin{bmatrix} \mathbf{S} + (\mathbf{P}_{\mathrm{ms}}\mathbf{B})^{\mathrm{T}}\mathbf{C}_{\mathrm{ha}}\mathbf{B} & (\mathbf{P}_{\mathrm{ms}}\mathbf{B})^{\mathrm{T}}\mathbf{C}_{\mathrm{hi}} \\ \mathbf{L}^{\mathrm{T}}\mathbf{C}_{\mathrm{ua}}\mathbf{B} & \mathbf{L}^{\mathrm{T}}\mathbf{C}_{\mathrm{ui}} + \mathbf{Z} \end{bmatrix} \begin{bmatrix} \mathbf{a} \\ \tilde{\mathbf{i}} \end{bmatrix} = \begin{bmatrix} -(\mathbf{P}_{\mathrm{ms}}\mathbf{B})^{\mathrm{T}}\mathbf{c}_{\mathrm{h}} \\ -\mathbf{L}^{\mathrm{T}}\mathbf{c}_{\mathrm{u}} + \mathbf{u}_{\mathrm{s}} \end{bmatrix} \tag{15}$$

of size $N_{\mathrm{m}} + N_{\mathrm{i}}$. Indeed, the contribution of the entire slave domain has been compressed into the $\mathbf{C}$ matrices and vectors. Problem (15) is often an order of magnitude smaller than the full problem with the slot included. Admittedly, the $\mathbf{C}$ matrices are in general full, which results in a dense sub-block of size $n_{\mathrm{mb}} \times n_{\mathrm{mb}}$ in the final system matrix. Nevertheless, it is still typically much faster to solve than the full problem, as shall be demonstrated later in the examples.

B. Deriving the Decoupling Matrices

Next, the matrices $\mathbf{C}_{\mathrm{ha}}, \mathbf{C}_{\mathrm{hi}}, \mathbf{C}_{\mathrm{ua}}, \mathbf{C}_{\mathrm{ui}}$ and vectors $\mathbf{c}_{\mathrm{h}}$, $\mathbf{c}_{\mathrm{u}}$ are derived. We begin by realizing that the slave domain forms a linear time-invariant (LTI) system (6)–(8). As such, it is fully characterized by its impulse response function. In other words, $\tilde{\mathbf{a}}$ and $\tilde{\mathbf{u}}$ are fully determined by the values of $\partial\tilde{\mathbf{a}}$ and $\tilde{\mathbf{i}}$ (both present and past). Specifically, due to the linearity, the superposition principle can be utilized: the contribution from each of the boundary node potentials $\partial\tilde{\mathbf{a}}_i$ and current $\tilde{\mathbf{i}}_i$ can be determined separately (while keeping the rest at zero), and then summed together.

To arrive at (13), the main-side boundary potentials $\partial\mathbf{a}$ and currents $\tilde{\mathbf{i}}$ are regarded as inputs to the impulse response function. Correspondingly, the Lagrange multipliers $\mathbf{h}$ and voltages $\tilde{\mathbf{u}}$ are the outputs. For example, the response of $\mathbf{h}$ to an impulse in $\partial\mathbf{a}$ can be written as

$$\mathbf{H}_{\mathrm{a}}^{\mathrm{I}}(t) = \begin{bmatrix} \mathbf{h}_{\mathrm{a}1}^{\mathrm{I}}(t) & \mathbf{h}_{\mathrm{a}2}^{\mathrm{I}}(t) & \dots & \mathbf{h}_{\mathrm{a}N^{\mathrm{cpl}}}^{\mathrm{I}}(t) \end{bmatrix}. \tag{16}$$

Here, each $\mathbf{h}_{\mathrm{a}i}^{\mathrm{I}}(t)$ denotes the continuous-time response of $\mathbf{h}$ to an impulse in the boundary potential i. It can be obtained by first solving (6) – (8) (of size $N_{\mathrm{s}} + N_{\mathrm{u}}$) in the time-domain with the time-dependent boundary data

$$\partial\tilde{\mathbf{a}}(t) = \mathbf{P}_{\mathrm{ms}}\partial\mathbf{a}^{\delta}(t) \tag{17}$$

$$\tilde{\mathbf{i}} \equiv \mathbf{0}, \tag{18}$$

where

$$\partial\mathbf{a}_j^{\delta}(t) = \begin{cases} \delta(t) & \text{if } j = i \\ 0 & \text{otherwise,} \end{cases} \tag{19}$$

and $\delta(t)$ is the unit impulse function. Once the solution has been computed, $\mathbf{h}$ can easily obtained in the post-processing stage by multiplying the second row of (12) by $\tilde{\mathbf{B}}$ and solving for $\mathbf{h}$.

Using a similar notation, let us also define the impulse response functions $\mathbf{H}_{\mathrm{i}}^{\mathrm{I}}(t)$. These are the responses of $\mathbf{h}$ to an impulse in one of the currents $\tilde{\mathbf{i}}$, while keeping $\partial\tilde{\mathbf{a}} \equiv \mathbf{0}$. Finally, let us treat the voltages $\tilde{\mathbf{u}}$ in a similar fashion, and denote their responses to $\partial\mathbf{a}$ and $\tilde{\mathbf{i}}$ by $\mathbf{U}_{\mathrm{a}}^{\mathrm{I}}(t)$ and $\mathbf{U}_{\mathrm{i}}^{\mathrm{I}}(t)$ respectively.

With the impulse response functions, $\mathbf{h}$ and $\tilde{\mathbf{u}}$ at any point t in time can be obtained with a convolution

$$\begin{aligned} \mathbf{h}(t) &= \int_0^t \left[\mathbf{H}_{\mathrm{a}}^{\mathrm{I}}(t-\tau)\partial\mathbf{a}(\tau) + \mathbf{H}_{\mathrm{i}}^{\mathrm{I}}(t-\tau)\tilde{\mathbf{i}}(\tau)\right] \mathrm{d}\tau \qquad (20) \\ &= \mathbf{H}_{\mathrm{a}}^{\mathrm{I}} *_0^t \partial\mathbf{a} + \mathbf{H}_{\mathrm{i}}^{\mathrm{I}} *_0^t \tilde{\mathbf{i}} \\ \tilde{\mathbf{u}}(t) &= \mathbf{U}_{\mathrm{a}}^{\mathrm{I}} *_0^t \partial\mathbf{a} + \mathbf{U}_{\mathrm{i}}^{\mathrm{I}} *_0^t \tilde{\mathbf{i}}. \qquad (21) \end{aligned}$$

This fact can then be utilized in time-stepping analysis as follows. The continuous-time solution $\partial\mathbf{a}(t)$ can be written as

$$\partial\mathbf{a}(t) = \sum_k \partial\mathbf{a}^k l^k(t), \tag{22}$$

where $\partial\mathbf{a}^1, \partial\mathbf{a}^2, \dots$ are the solutions at each time-step, and $l(t)$ are some scalar-valued, piece-wise continuous functions of time satisfying

$$l^k(t) = \begin{cases} 1 & t = t^k \\ 0 & t = t^i \text{ for any } i \neq k. \end{cases} \tag{23}$$

The same holds for the currents $\tilde{\mathbf{i}}(t)$. The exact form of l depends on the time-stepping scheme used – e.g. the backward-Euler method would correspond to piecewise-constant l.

At the time-step $k+1$, the values of $\partial\mathbf{a}$ and $\tilde{\mathbf{i}}$ are only known up to k. Hence, we can split the convolution into two parts, and write

$$\begin{aligned} \mathbf{h}^{k+1} = &\left(\mathbf{H}_{\mathrm{a}}^{\mathrm{I}} *_{t^k}^{t^{k+1}} \mathbf{I}l^{k+1}\right)\partial\mathbf{a}^{k+1} + \left(\mathbf{H}_{\mathrm{i}}^{\mathrm{I}} *_{t^k}^{t^{k+1}} \mathbf{I}l^{k+1}\right)\tilde{\mathbf{i}}^{k+1} \\ &+ \mathbf{H}_{\mathrm{a}}^{\mathrm{I}} *_0^{t^k} \left(\sum_{l=1}^{k} \partial\mathbf{a}^l l^l\right) + \mathbf{H}_{\mathrm{i}}^{\mathrm{I}} *_0^{t^k} \left(\sum_{l=1}^{k} \tilde{\mathbf{i}}^l l^l\right), \end{aligned} \tag{24}$$

where $\mathbf{I}$ is the identity matrix. Now we see that this expression corresponds to (13), with the first line representing the two

matrix terms and the second line corresponding to the vector. The voltages $\tilde{\mathbf{u}}$ can be treated equivalently.

1) Constant Time-Step Length

The above is valid for a general time-dependency. However, it can be considerably simplified if a constant time-step length Δt is assumed. In this case, the decomposition approach will yield *exactly* the same solution as solving the original problem would, up to numerical accuracy.

We begin by replacing the impulse function δ by its discrete equivalent

$$\delta_{\mathrm{d}}^{k} = \begin{cases} 1 & k = 1 \\ 0 & \text{otherwise.} \end{cases} \tag{25}$$

Equivalently to (16), the impulse response functions are replaced by their discrete-time equivalents

$$\mathbf{H}_{\mathrm{a}}^{\mathrm{I}\,k} = \left[\mathbf{h}_{\mathrm{a}1}^{\mathrm{I}\,k} \quad \mathbf{h}_{\mathrm{a}2}^{\mathrm{I}\,k} \quad \dots \quad \mathbf{h}_{\mathrm{a}N^{\mathrm{cpl}}}^{\mathrm{I}\,k} \right], \tag{26}$$

i.e. sets of matrices. These can be easily computed numerically by starting from all-zero initial conditions at $k = 0$. Finally, the convolutions are replaced by discrete convolutions, i.e.

$$\begin{aligned} \mathbf{h}^{k+1} = {} & \mathbf{H}_{\mathrm{a}}^{\mathrm{I}\,1} \partial \mathbf{a}^{k+1} + \mathbf{H}_{\mathrm{i}}^{\mathrm{I}\,1} \tilde{\mathbf{i}}^{k+1} \\ & + \sum_{l=1}^{k} \left(\mathbf{H}_{\mathrm{a}}^{\mathrm{I}\,k-l+2} \partial \mathbf{a}^{l} + \mathbf{H}_{\mathrm{i}}^{\mathrm{I}\,k-l+2} \tilde{\mathbf{i}}^{l} \right) \end{aligned} \tag{27}$$

and similarly for $\tilde{\mathbf{u}}$. In practice, the impulse responses will often decay to zero in a few time-steps. In this case, they can be truncated, so the summation begins at some $l > 1$.

2) Variable Time-Step Length

In the case of a variable time-step length, discrete-time analysis cannot be utilized. Thus, approximate impulse response functions have to be obtained by numerical means. Similarly, the convolutions have to be computed as integrals, rather than finite sums. Otherwise, the basic principles remain unchanged.

C. General Workflow of the Proposed Method

For clarity, the workflow of the proposed method has been illustrated in Fig. 2, for a fixed time-step length. The problem domain is first divided into the main and slave parts, and both are meshed independently. The impulse responses of the slave domain are computed, utilizing the boundary nodes of the main mesh as per (17). Once the response computation is finished, the system (15) is assembled, with the help of (27).

Next, time-stepping analysis can be performed. At each step, the load-vector side of (15) is updated by computing the convolution term of (27). The nonlinear problem is then solved with the Newton-Raphson method. After the time-stepping, typical post-processing tasks can be performed.

D. Non-zero Initial Conditions

Until now, zero initial conditions have been assumed. However, time-stepping analysis of electrical machines is often started from the conditions obtained from harmonic analysis, instead. Two approaches are next proposed for this situation.

The first one is to compute an additional zero-input decay term. In other words, $\mathbf{h}_{\text{decay}}(t)$ and $\tilde{\mathbf{u}}_{\text{decay}}(t)$ are pre-computed with initial conditions corresponding to the harmonic analysis

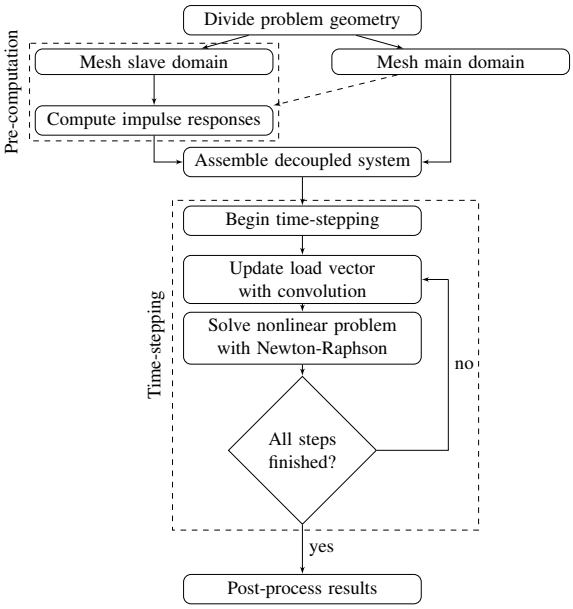

Fig. 2. Flowchart of the proposed method.

solution, with $\partial \mathbf{a}$ and $\tilde{\mathbf{i}}$ set to zero for all $t > 0$. The final $\mathbf{h}$ and $\tilde{\mathbf{u}}$ will then be a sum of this decay term, plus the convolution term described in the previous Section.

Another solution is to extend $\partial \mathbf{a}(t)$ and $\tilde{\mathbf{i}}(t)$ to $t < 0$ by using a sinusoidal time-dependency corresponding to the harmonic solution. Obviously, the convolution then has to be started from negative time, too. Additionally, the solution obtained by this method will not generally be exactly the same as given by the first approach, as the contribution of the $t < 0$ conditions are handled in a different way. The accuracy of both approximations will be evaluated in the results section.

E. Harmonic Analysis and Nonlinearity

The proposed method can very easily be applied to time-harmonic analysis as well, with two minor changes. The impulse response function is replaced by a complex single-frequency response [24], [26]. Additionally, computing the convolution is no longer necessary.

Likewise, nonlinear problems can easily be solved with the Newton-Raphson method. Since the slots are linear, their contribution to the Jacobian

$$\mathbf{J} = \frac{\partial \left(\mathbf{S} \left(\mathbf{a} \right) \mathbf{a} \right)}{\partial \mathbf{a}} = \mathbf{S} + \frac{\partial \mathbf{S}}{\partial \mathbf{a}} \tag{28}$$

is limited to the first term $\mathbf{S}$ only.

F. Several Slots and 3D Problems

The proposed approach should prove increasingly more powerful in practical problems that contain several slots. Since the slots are typically geometrically identical, the same impulse response functions can be utilized for all of them. To take into account the fact that the slot currents $\tilde{\mathbf{i}}_j$ for a particular slot j are a linear function $\tilde{\mathbf{i}}_j = \mathbf{L}_j \mathbf{i}$ of the main problem currents $\mathbf{i}$, all slave-domain strands can be assumed parallel-connected in the pre-computation stage. This has the

added benefit that different winding configurations can be analysed by simply changing $\mathbf{L}$. Likewise, only a subset $\partial\mathbf{a}_j$ of the main problem boundary potentials will be used as input for each slot.

Of course, this is not valid if the geometry of the slots differs, e.g. due to a different packing of conductors. In this case, separate functions must be computed for each slot. However, based on the simulation results presented later, this should still have a relatively minor effect on total computation time. Furthermore, a stochastic response-surface approach could probably further decrease the computational cost, as the exact packing is in reality uncertain.

The method *appears* applicable to 3D problems, as Lagrange multipliers are often used in them as well. The impulse response-convolution approach also works, as the slots and conductors are still LTI systems. However, a numerical verification is of course sorely needed, as is analysis of the computational benefits.

G. Eddy Current Loss Computation

It must be noted that the methodology presented so far is not sufficient for computing the total resistive losses. Indeed, for that purpose also the vector potential $\tilde{\mathbf{a}}(t)$ has to be known at least in the conductive parts of the slave domain, in addition to $\tilde{\mathbf{u}}(t)$.

This problem can be solved by storing also $\tilde{\mathbf{a}}$ when computing the impulse response functions of $\tilde{\mathbf{u}}$ and $\mathbf{h}$. If memory becomes an issue, the values can be stored on the hard drive as they are only needed in the post-processing stage. Then, both $\tilde{\mathbf{a}}$ and $\tilde{\mathbf{u}}$ can be obtained from $\partial\mathbf{a}$ and $\mathbf{i}$ with the earlier-described convolution approach. From these, the current densities and losses can be easily computed.

H. Comparison to Previous Approaches

Some comparison to previously-published winding modelling approaches is probably in order. The proposed method has been heavily inspired by the approach in [24], where a Dirichlet-to-Neumann mapping was also used for coupling between the problem domains. In this method, the slave domain comprised a single conductor only. This obviously reduces the pre-computation cost, but correspondingly also increases the number of unknowns in the full problem. Also, a regular packing of conductors is needed for this approach to work. Furthermore, it appears that the Neumann-side of the boundary coupling was implemented in the continuous sense. This can introduce additional error into the solution, as the Neumann boundary condition is only satisfied in the weak sense. Finally, the analysis was limited to time-harmonic problems only, although extension to time-domain could be handled in a similar way as here.

A somewhat different approach was used by the authors in [26]. Rather than using Lagrange multipliers, a set of slave domain solutions $\mathbf{A} = \begin{bmatrix}\tilde{\mathbf{a}}_1 & \tilde{\mathbf{a}}_2 & \dots & \tilde{\mathbf{a}}_{N^{\mathrm{cpl}}}\end{bmatrix}$ was stored, each corresponding to a different Dirichlet boundary conditions via $\partial\mathbf{a}$. The pre-computed solutions were then used as shape functions in the main problem, resulting in the appearance of reduced matrices of type $\hat{\mathbf{S}} = \mathbf{A}^{\mathrm{T}}\tilde{\mathbf{S}}\mathbf{A}$. This approach would also yield an exact solution. However, extending it to time-domain would require storing the impulse response function of entire $\tilde{\mathbf{a}}$, and re-computing large matrix-vector products of type $\tilde{\mathbf{S}}\tilde{\mathbf{a}}$ at each time-step.

It must be noted that in [26], the concept of *coupling nodes* was introduced. These were an extra set of unknowns, defined on the main-slave boundary and shown to improve calculation accuracy in some conditions. If required, they can also straightforwardly applied to the method proposed here as well. Indeed, the presented approach is a special case of the coupling node methodology, with the coupling nodes corresponding to the main-mesh boundary nodes.

IV. Simulations

To evaluate the proposed method, a random-wound 500 kW four-pole induction machine was used as a test problem. The machine had a double-layer winding with four parallel paths. The other main dimensions can be found in Table I, and the cross-section in Fig. 3. Since the machine had a large symmetry sector of 48 stator slots, the problem had a total of 5376 conductors in the stator alone. The uncertainty inherent in random-wound windings was not modelled, i.e. the winding configuration was regarded as fully known.

TABLE I
Main Dimensions of the Machine.

Rated frequency (Hz)	50
Slip (%)	0.637
Number of winding layers	2
Number of strands per slot	112
Number of turns	2
Number of stator slots	96
Number of rotor slots	74
Stator diameter (mm)	600
Length (mm)	760

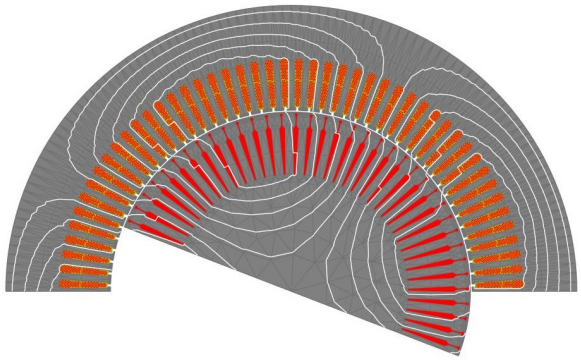

Fig. 3. Cross-section of the machine and flux lines at $t = 38$ ms in the sinusoidal supply simulation.

The main domain, i.e. the cross-section of the machine excluding the stator slots, was meshed with 4766 first-order triangular elements, corresponding to 3319 nodes. For the slot domain, an approximately hexagonal packing was generated for the strands, resulting in the slot mesh illustrated in Fig. 4. The impulse response functions were then computed and stored.

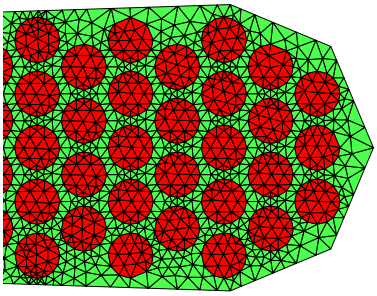

Fig. 4. Part of the slot mesh used in the simulations.

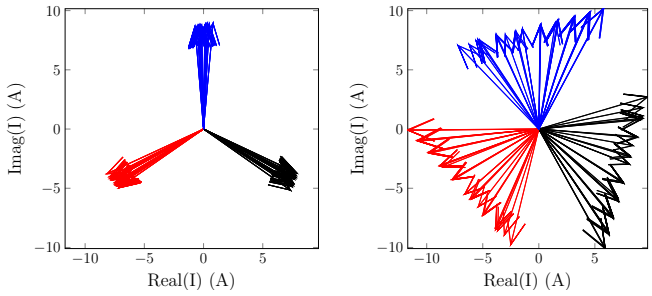

(a) (b)

Fig. 5. Current phasors of all stator current loops of the machine, with the good (a) and bad (b) winding configurations. Phases are denoted with the different colors. For clarity, the same scale is used in both subfigures.

To obtain a reference solution at a tolerable computational cost, a non-conforming meshing approach was chosen. Most commonly used for modelling motion, these approaches have been used for decades, and their accuracy studied and demonstrated (e.g. [32]–[34]). Indeed, the reference solution mesh was formed as the union of the main domain mesh, and the slave domain mesh replicated and rotated to cover all 48 slots. The continuity of the solution was enforced with the polynomial interpolation approach [28]. This way, the density of the mesh could change sharply over the slot boundary, limiting the number of nodes to roughly 150 000. Even so, the problem size was on the upper limit for direct linear solvers on typical desktops.

A. Focus of Analysis

It must be emphasized that each parallel path of the machine consisted of 28 strands connected in parallel. Thus, circulating currents - uneven division of the total current between the parallel strands - could be of special interest. For this purpose, the circulating current factor will be used

$$k_{\mathrm{cc}} = \frac{N \sum_{k=1}^{N} i_k^2}{\left(\sum_{k=1}^{N} i_k \right)^2} - 1 \tag{29}$$

to quantify the relative increase in resistive losses due to circulating currents, in each parallel path [35]. The number of parallel current loops has been denoted by N, and the loop currents by i_k.

Furthermore, the term *loop* current will be used to denote the current flowing in a set of strands connected in series. By contrast, the term *path* shall refer to the four parallel paths in each phase. In other words, the total current of each path would be the sum of 28 loop currents.

Finally, two different strand configurations were analyzed. In the "good" one, the strands were fully transposed between slots. In other words, a strand on the bottom of a layer in one slot would be on the top of the layer in the next one. Thus, the loop matrix $\mathbf{L}$ consisted of diagonal and counter-diagonal blocks, and zero blocks. By contrast, in the "bad" configuration the relative positions were unchanged, and $\mathbf{L}$ had diagonal blocks only.

B. Time-Harmonic Analysis

The machine was first analyzed with harmonic analysis, using the good strand configuration. The nonlinear problem was solved with the Newton-Raphson method, by splitting it into its real and imaginary components [36]. With both methods, the iteration converged in 15 steps to the rather strict relative residual norm of $< 10^{-9}$.

A comparison of the computational times can be found in Table II. The number of free variables, with all continuity conditions eliminated, is also shown. As can be seen, the reference solution took more than 100 times longer compared to the proposed approach, with the majority of the time spent on solving the large linear problems. With the proposed method, roughly 28 % of the total time was spent on pre-computation. Obviously, this ratio would probably be larger if a more forgiving tolerance had been used for convergence, decreasing the number of iterations.

TABLE II
COMPUTATIONAL COSTS IN HARMONIC ANALYSIS.

	Proposed Method	**Reference**
No. of unknowns	6824	372 008
Total computation time	3.20 s	4 min 17.46 s
• Pre-computation	0.70 s	-
• Jacobian factorization	1.67 s	3 min 14.52 s

As expected, the results from both methods were very close to each other. Indeed, the discrete error norms of the main-mesh nodal potentials, rotor voltages, and stator loop currents were 2.68×10^{-12}, 5.02×10^{-13}, and 1.78×10^{-11} respectively. These minor differences can probably be attributed to the finite floating-point precision, causing the nonlinear iterations to converge to slightly different points.

Fig. 5(a) shows the current phasors for all parallel current paths in the machine. Phase (a) is denoted by the black color, and phases (b) and (c) with red and blue, respectively. As can be seen, the total phase currents were almost evenly divided between the strands. Indeed, the circulating current factor for each path was only 0.23 %. This conforms to the common assumption that stranded windings can be modelled by a uniform equivalent current density.

However, this changed when the winding configuration was changed to the bad one. As can be seen in Fig. 5(b), there

were now major differences between different current loops. Indeed, the circulating current factor was now equal to 21 %.

Obviously, the latter situation was unrealistically bad as some kind of strand transposition is usually employed in practice. Nevertheless, it demonstrated how circulating currents could be a significant loss component even in large machines supplied by grid-frequency, and thus have to be considered in the winding design and manufacture.

C. Time-Stepping Analysis with Sinusoidal Supply

Next, time-stepping analysis was performed using a sinusoidal supply voltage. Two periods were analyzed, with a relatively modest 200 time-steps per period. Rotor rotation was modelled with the moving band technique [37]. The backward Euler method was used, and the time-step length was fixed. The number of Newton iterations was fixed to 5, which was enough to ensure convergence to a relative residual norm of $10^{-10}...10^{-9}$. A variable number of iterations was also tested, but it was found to cause minor differences ($< 10^{-5}$) in the convergence behaviour of the two methods.

With the proposed method, the impulse response functions were truncated once they had decayed to the level of the machine epsilon 10^{-15}. 15 time-steps were needed for this. The non-zero initial conditions were handled by computing the decay term described in Section III-D.

A comparison of computation times can again be found in Table III. It can be seen that the proposed method was approximately 73 times faster. The on-line computation time was again mostly spent on solving the linear systems. Neither the pre-computation nor computing the discrete convolutions took significant amounts of time.

TABLE III
COMPUTATIONAL COSTS IN TIME-STEPPING ANALYSIS.

	Proposed Method	**Reference**
Total computation time	1 min 52 s	2 h 12 min
• Pre-computation	3.10 s	-
• Convolution	5.87 s	-
• Jacobian factorization	1 min 6 s	1 h 28 min

The accuracy of the proposed method is illustrated in Fig. 6. Shown are the range of absolute differences of loop currents between the proposed method and the reference solution, i.e. $\max_j \left[|\mathbf{i} - \mathbf{i}_{\text{ref}}|\right]_j$ and $\min_j \left[|\mathbf{i} - \mathbf{i}_{\text{ref}}|\right]_j$ for each time-step. As can be seen, even the highest deviations are negligible compared to the rms values of several Amperes in each current loop. No differences were found in the convergence of the nonlinear iteration, and no particular current loop was more prone to higher errors than the others.

Fig. 7 shows the total resistive losses in the stator, i.e. losses due to circulating currents plus skin- and proximity effects both. For clarity, the losses have been presented both as absolute values, and as a relative increase from the RI^2 losses computed from the phase currents and DC resistances. As can be seen, both additional loss components were almost negligible, with circulating currents contributing only 11 W and other eddy current effects 25 W on average, respectively. Compared

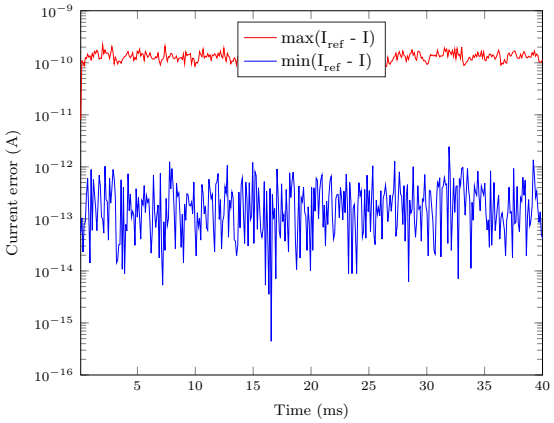

Fig. 6. Differences of loop currents obtained from the two methods, as functions of time.

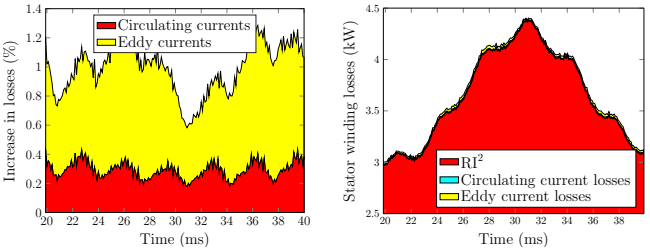

(a) (b)

Fig. 7. Additional losses due to circulating and eddy currents as functions of time (a) as relative increases from the RI^2 approximation (b) absolute values.

to the RI^2 losses of 3.6 kW, their relative contributions were only 0.28 % and 0.70 % respectively.

A much larger effect was seen with the bad winding configuration. The circulating losses were increased to 740 W, corresponding to a 20.3 % addition to the RI^2 losses. The eddy current losses remained almost unchanged. Otherwise, the behaviour was similar to Fig. 7.

D. Time-Stepping Analysis with PWM Supply

The simulations were then repeated using a simplified pulse-width modulated (PWM) voltage supply. The voltage waveforms were generated using the well-known sine-triangle comparison with a switching frequency of 2 kHz and modulation and amplitude indices of $\pi/4$ and 1, respectively. To limit aliasing due to the finite time-step length, the average input voltage for each time-step was used instead of the instantaneous value. The number of time-steps was set to 800 per period, translating to roughly 10 steps per the second switching harmonics around 4 kHz.

Fig. 8(a) again shows the current errors between the two methods as a function of time. Again, the errors were very small, staying below 10^{-9}. The total computation time was 9 h 55 min for the reference solution and 7 min 3 s for the proposed approach, corresponding to an 85-fold speed-up.

This time, also the harmonic approach of Section III-D was evaluated for modeling the initial conditions. The corresponding current errors are shown in Fig. 8(b). As can be seen, the

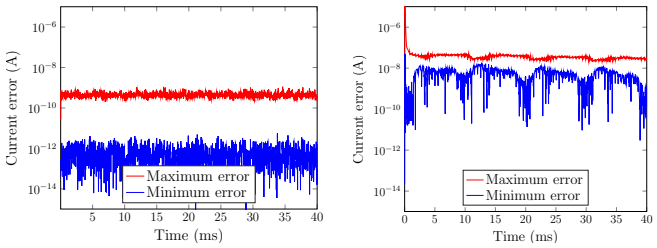

Fig. 8. Differences of loop currents obtained from the two methods, as functions of time. Initial conditions were handled with the decay function approach in (a), and the harmonic approximation in (b).

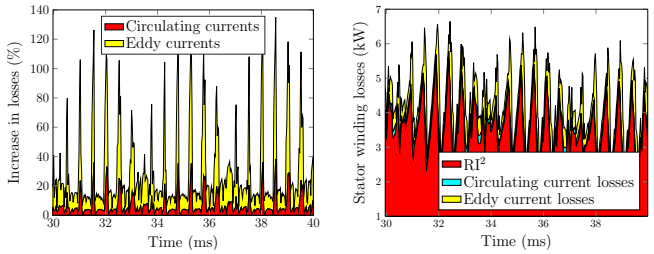

Fig. 10. Additional losses due to circulating and eddy currents as functions of time (a) as relative increases from the RI^2 approximation (b) absolute values.

harmonic method was roughly two orders of magnitude less accurate compared to the decay-term method. However, the errors were still very small compared to e.g. the rms values of the loop currents

Fig. 9 then shows the simulated phase currents. As can be seen, the PWM supply caused considerable ripple in the currents. The effect on losses was also pronounced, as is evident from Fig. 10. The average resistive stator losses were 4.2 kW, of which 202 W and 712 W were caused by circulating and eddy currents. These correspond to 6.1 % and 21.4 % increases from the RI^2 losses respectively. Both terms varied significantly with time, peaking immediately after the supply voltage switches.

Shifting to the bad winding configuration resulted in much more pronounced loss increase than with sinusoidal supply. The total losses were increased to 7.2 kW, of which 3.4 kW was due to circulating currents. Eddy current losses again remained roughly the same, and the behaviour was otherwise similar to Fig. 10.

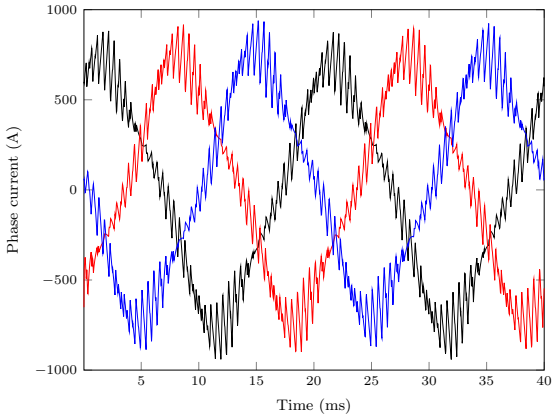

Fig. 9. Phase currents with PWM supply.

E. Comparison to an Established Approach

Finally, the PWM supply case was re-analysed with a more widespread approach. The stator winding, being stranded after all, was modelled with a uniform current density. The eddy current losses were then estimated in the post-processing stage with the squared-field derivative (SFD) method [38]. Obviously, both the circulating currents and the effect of strand transpositions (good versus bad winding) were ignored. The computation time was 3 min 55 s.

The computed loss distributions are compared in Table IV, with the same loss components again considered. The post-processing approach appears reasonably accurate if the circulating are suppressed by the strand transpositions (good winding). However, it is clearly insufficient for problems with significant circulating currents (bad winding).

TABLE IV
COMPARISON OF THE LOSSES.

	P_{DC} (W)	$P_{\mathrm{circ.}}$ (W)	P_{eddy} (W)
Squared-field derivative	3222	0	887
Proposed (good winding)	3324	202	712
Proposed (bad winding)	3347	3391	416

V. CONCLUSION

An efficient numerical approach is proposed for time-domain analysis of winding losses in electrical machines. The slots are modelled with their pre-computed impulse response functions and coupled together with the rest of the problem domain on the boundary. The method can be used on windings of arbitrary configuration and considers all resistive AC loss components. Under suitable conditions, it will yield results very close to those obtained via traditional finite element analysis. Finally, similar methodology can also be used for time-harmonic analysis.

The proposed method was evaluated by simulating a 500 kW induction machine with a stranded stator winding. The method yielded precise results in both time-harmonic and time-stepping analysis. Compared to the reference solution obtained by normal FE analysis, the proposed method was more than 100 times faster in the harmonic case, and 70–85 times faster in time-stepping. The convergence behaviour of the nonlinear iteration was identical to the reference solution.

According to the simulations, the analyzed machine exhibits very small additional resistive losses in the stator, *if* the parallel strands are transposed between slots and the machine is supplied with a sinusoidal voltage. However, without any transpositions, the circulating currents increase the losses considerably. The situation is exacerbated if PWM supply is used.

Some further work is still required. The method should be implemented and verified with second-order FE basis functions, as they are commonly used in analysis of electrical machines. 3D analysis could also be tested. Additionally, statistical analysis of the AC losses could be of interest, as the winding topology of a random-wound machine is indeed uncertain.

ACKNOWLEDGMENT

The research leading to these results has received funding from the European Research Council under the European Union's Seventh Framework Programme (FP7/2007-2013) / ERC Grant Agreement n. 339380.

REFERENCES

[1] J. Gyselinck and P. Dular, "Frequency-domain homogenization of bundles of wires in 2-D magnetodynamic FE calculations," *IEEE Trans. Magn.*, vol. 41, no. 5, pp. 1416–1419, May 2005.

[2] J. Gyselinck, P. Dular, N. Sadowski, P. Kuo-Peng, and R. Sabariego, "Homogenization of form-wound windings in frequency and time domain finite-element modeling of electrical machines," *IEEE Trans. Magn.*, vol. 46, no. 8, pp. 2852–2855, Aug 2010.

[3] R. Sabariego, P. Dular, and J. Gyselinck, "Time-domain homogenization of windings in 3-D finite element models," *IEEE Trans. Magn.*, vol. 44, no. 6, pp. 1302–1305, June 2008.

[4] J. Gyselinck, R. Sabariego, and P. Dular, "Time-domain homogenization of windings in 2-D finite element models," *IEEE Trans. Magn.*, vol. 43, no. 4, pp. 1297–1300, April 2007.

[5] Z. De Greve, O. Deblecker, J. Lobry, and J.-P. Keradec, "High-frequency multi-winding magnetic components: From numerical simulation to equivalent circuits with frequency-independent RL parameters," *IEEE Trans. Magn.*, vol. 50, no. 2, pp. 141–144, Feb 2014.

[6] J. Sibue, J. Ferrieux, G. Meunier, and R. Periot, "Modeling of losses and current density distribution in conductors of a large air-gap transformer using homogenization and 3-D FEM," *IEEE Trans. Magn.*, vol. 48, no. 2, pp. 763–766, Feb 2012.

[7] J.-R. Sibue, G. Meunier, J.-P. Ferrieux, J. Roudet, and R. Periot, "Modeling and computation of losses in conductors and magnetic cores of a large air gap transformer dedicated to contactless energy transfer," *IEEE Trans. Magn.*, vol. 49, no. 1, pp. 586–590, Jan 2013.

[8] X. Nan and C. Sullivan, "An equivalent complex permeability model for Litz-wire windings," *IEEE Trans. Ind. Appl.*, vol. 45, no. 2, pp. 854–860, March 2009.

[9] Z. D. Grve, P. Dular, J. Gyselinck, C. Geuzaine, O. Deblecker, and J. Lobry, "Refinement of homogenized magnetodynamic models of wound inductors using finite-element subproblems," *IEEE Trans. Magn.*, vol. 51, no. 3, pp. 1–4, March 2015.

[10] A. Lehikoinen, N. Chiodetto, E. Lantto, A. Arkkio, and A. Belahcen, "Monte Carlo analysis of circulating currents in random-wound electrical machines," *IEEE Trans. Magn.*, vol. 52, no. 8, pp. 1–12, Aug 2016.

[11] A. Lehikoinen and A. Arkkio, "Efficient finite element computation of circulating currents in thin parallel strands," *IEEE Trans. Magn.*, vol. PP, no. 99, pp. 1–1, 2015.

[12] M. van der Geest, H. Polinder, J. Ferreira, and D. Zeilstra, "Current sharing analysis of parallel strands in low-voltage high-speed machines," *IEEE Trans. Ind. Electron.*, vol. 61, no. 6, pp. 3064–3070, June 2014.

[13] F. Jiancheng, L. Xiquan, B. Han, and K. Wang, "Analysis of circulating current loss for high-speed permanent magnet motor," *IEEE Trans. Magn.*, vol. 51, no. 1, pp. 1–13, Jan 2015.

[14] I. Petrov, M. Polikarpova, P. Ponomarev, P. Lindh, and J. Pyrhönen, "Investigation of additional AC losses in tooth-coil winding PMSM with high electrical frequency," in *2016 XXII International Conference on Electrical Machines (ICEM)*, Sept 2016, pp. 1841–1846.

[15] R. Wrobel, D. Staton, R. Lock, J. Booker, and D. Drury, "Winding design for minimum power loss and low-cost manufacture in application to fixed-speed PM generator," *IEEE Trans. Ind. Appl.*, vol. 51, no. 5, pp. 3773–3782, Sept 2015.

[16] M. Fujita, Y. Kabata, T. Tokumasu, K. Nagakura, M. Kakiuchi, and S. Nagano, "Circulating currents in stator coils of large turbine generators and loss reduction," *IEEE Trans. Ind. Appl.*, vol. 45, no. 2, pp. 685–693, March 2009.

[17] M. Islam, S. Mir, and T. Sebastian, "Effect of paralleling the stator coils in a permanent-magnet machine," *IEEE Trans. Ind. Appl.*, vol. 42, no. 6, pp. 1429–1436, Nov 2006.

[18] M. Vetuschi and F. Cupertino, "Minimization of proximity losses in electrical machines with tooth-wound coils," *IEEE Trans. Ind. Appl.*, vol. 51, no. 4, pp. 3068–3076, July 2015.

[19] A. Tessarolo, F. Agnolet, F. Luise, and M. Mezzarobba, "Use of time-harmonic finite-element analysis to compute stator winding eddy-current losses due to rotor motion in surface permanent-magnet machines," *IEEE Trans. Energy Convers.*, vol. 27, no. 3, pp. 670–679, Sept 2012.

[20] S. Iwasaki, R. P. Deodhar, Y. Liu, A. Pride, Z. Q. Zhu, and J. J. Bremner, "Influence of PWM on the proximity loss in permanent-magnet brushless AC machines," *IEEE Trans. Ind. Appl.*, vol. 45, no. 4, pp. 1359–1367, July 2009.

[21] Y. Amara, P. Reghem, and G. Barakat, "Analytical prediction of eddy-current loss in armature windings of permanent magnet brushless AC machines," *IEEE Trans. Magn.*, vol. 46, no. 8, pp. 3481–3484, Aug 2010.

[22] L. J. Wu, Z. Q. Zhu, D. Staton, M. Popescu, and D. Hawkins, "Analytical model of eddy current loss in windings of permanent-magnet machines accounting for load," *IEEE Trans. Magn.*, vol. 48, no. 7, pp. 2138–2151, July 2012.

[23] A. G. Sarigiannidis and A. G. Kladas, "Switching frequency impact on permanent magnet motors drive system for electric actuation applications," *IEEE Trans. Magn.*, vol. 51, no. 3, pp. 1–4, March 2015.

[24] L. Lehti, J. Keranen, S. Suuriniemi, and L. Kettunen, "Coil winding losses: Decomposition strategy," *IEEE Trans. Magn.*, vol. 52, no. 1, pp. 1–6, Jan 2016.

[25] I. A. Tsukerman, A. Konrad, and J. D. Lavers, "A method for circuit connections in time-dependent eddy current problems," *IEEE Trans. Magn.*, vol. 28, no. 2, pp. 1299–1302, Mar 1992.

[26] A. Lehikoinen, A. Arkkio, and A. Belahcen, "Reduced basis finite element modelling of electrical machines with multi-conductor windings," in *2016 XXII International Conference on Electrical Machines (ICEM)*, September 2016, pp. 1–7.

[27] X. Shi, Y. L. Menach, J. P. Ducreux, and F. Piriou, "Comparison between the mortar element method and the polynomial interpolation method to model movement in the finite element method," *IEEE Trans. Magn.*, vol. 44, no. 6, pp. 1314–1317, June 2008.

[28] G. J. Wallinger and O. Bíró, "3-D FE method analysis of static fields for non-conforming meshes with second-order node-based elements," *IEEE Transactions on Magnetics*, vol. 52, no. 3, pp. 1–4, March 2016.

[29] H. D. Gersem and T. Weiland, "Harmonic weighting functions at the sliding interface of a finite-element machine model incorporating angular displacement," *IEEE Trans. Magn.*, vol. 40, no. 2, pp. 545–548, March 2004.

[30] R. Stenberg, "On some techniques for approximating boundary conditions in the finite element method," *Journal of Computational and applied Mathematics*, vol. 63, no. 1-3, pp. 139–148, 1995.

[31] I. Babuška, "The finite element method with lagrangian multipliers," *Numerische Mathematik*, vol. 20, no. 3, pp. 179–192, 1973.

[32] O. J. Antunes, J. P. A. Bastos, N. Sadowski, A. Razek, L. Santandrea, F. Bouillault, and F. Rapetti, "Comparison between nonconforming movement methods," *IEEE Trans. Magn.*, vol. 42, no. 4, pp. 599–602, April 2006.

[33] K. Muramatsu, T. Nakata, N. Takahashi, and K. Fujiwara, "Investigation of effectiveness of 3-d nonconforming mesh," *IEEE Trans. Magn.*, vol. 27, no. 6, pp. 5211–5213, Nov 1991.

[34] K. Muramatsu, Y. Yokoyama, N. Takahashi, A. Nafalski, and O. Gol, "Effect of continuity of potential on accuracy in magnetic field analysis using nonconforming mesh," *IEEE Trans. Magn.*, vol. 36, no. 4, pp. 1578–1582, Jul 2000.

[35] J. Lähteenmäki, "Design and voltage supply of high-speed induction machines," Ph.D. dissertation, Helsinki University of Technology, Espoo, Nov. 2002. [Online]. Available: http://lib.tkk.fi/Diss/2002/isbn951226224X/

[36] A. Arkkio, "Analysis of induction motors based on the numerical solution of the magnetic field and circuit equations," Ph.D. dissertation, Helsinki University of Technology, Espoo, Dec. 1987. [Online]. Available: http://lib.tkk.fi/Diss/198X/isbn951226076X/isbn951226076X.pdf

[37] B. Davat, Z. Ren, and M. Lajoie-Mazenc, "The movement in field modeling," *IEEE Trans. Magn.*, vol. 21, no. 6, pp. 2296–2298, Nov 1985.

[38] C. R. Sullivan, "Computationally efficient winding loss calculation with multiple windings, arbitrary waveforms, and two-dimensional or three-dimensional field geometry," *IEEE Trans. Power Electron.*, vol. 16, no. 1, pp. 142–150, Jan 2001.

Antti Lehikoinen was born in Joensuu, Finland, in 1988. He received the B.Sc. (Tech.) and M.Sc. degrees in electromechanics from the School of Electrical Engineering, Aalto University, Espoo, Finland, in 2012 and 2013, respectively, where he is currently pursuing the Ph.D. degree.

His current research interests include stochastic modeling and prediction of additional losses due to circulating currents in random-wound machines.

Jouni Ikäheimo (M12) was born in Seinäjoki, Finland, 1968. He received the M.Sc. and Ph.D. degrees in theoretical physics from Helsinki University of Technology, Espoo, Finland, in 1992 and 1996, respectively.

He has been working with electrical machines since 1996 at ABB Motors and Generators. Currently, he holds the position of Global Technology Manager for Low Voltage IEC motors. Before this appointment, he was the R&D manager for a local manufacturing unit at Vaasa.

Antero Arkkio was born in Vehkalahti, Finland in 1955. He received his M.Sc. (Tech.) and D.Sc. (Tech.) degrees from Helsinki University of Technology in 1980 and 1988. Currently he is a Professor of Electrical Engineering at Aalto University. His research interests deal with modeling, design, and measurement of electrical machines.

Anouar Belahcen (M13,SM'15) was born in Morocco, in 1963. He received the B.Sc. degree in physics from the University Sidi Mohamed Ben Abdellah, Fes, Morocco, in 1988 and the M.Sc. (Tech.) and Doctor (Tech.) degrees from Helsinki University of Technology, Finland, in 1998, and 2004, respectively. From 2008 to 2013, he has been working as Adjunct Professor in the field of coupled problems and material modeling at Aalto University, Finland. Since 2011 he is Professor of electrical machines at Tallinn University of Technology, Estonia and in 2013 he became Professor of Energy and Power at Aalto University. His research interests are numerical modeling of electrical machines, especially magnetic material modeling, coupled magnetic and mechanical problems, magnetic forces, and magnetostriction.